Radboud Repository

Radboud University Nijmegen

PDF hosted at the Radboud Repository of the Radboud University Nijmegen

The following full text is a publisher's version.

For additional information about this publication click this link.
http://hdl.handle.net/2066/23121

The Effect of Blood Flow on Oxygen Extraction Pressures Calculated in a Model of Pointlike Erythrocyte Sources for Rat Heart

LOUIS HOOFD AND CEES BOS
Department of Physiology, Faculty of Medical Sciences, University of Nijmegen, Geert Grooteplein Noord 21, 6525 EZ Nijmegen, The Netherlands

THOM OOSTENDORP
Department of Medical Physics and Biophysics, University of Nijmegen, Geert Grooteplein Noord 21, 6525 EZ Nijmegen, The Netherlands

---

ABSTRACT

A mathematical description of pericapillary oxygen gradients that takes into account the particulate nature of blood is possible in terms of erythrocytes as pointlike sources. The formulation in terms of quasi-stationary sources [1] is extended to account for moving erythrocytes. The extended model is semianalytical and can be used to estimate the extraction pressure (EP), which quantifies the effect on partial pressure of oxygen (pO_2) in the tissue far from the erythrocytes. Simulations have been done for rat heart muscle tissue around a capillary. For low hematocrit (Hct; 20%) and low blood velocity EP is highest, higher than the pO_2 drop in a surrounding typical tissue cylinder. This means that the impediment to O_2 release close to the capillary can be larger than that to transport further into the tissue. Increasing the hematocrit decreases EP, that is, it facilitates O_2 release. Increasing the blood velocity decreases EP at low Hct values but has the opposite effect at high Hct values ($> 35\%$). For zero velocity, results are the same as with the quasi-stationary model.

---

1. INTRODUCTION

Once oxygen is released from the capillary, modeling of its further transport into tissue is based on diffusion. The first model of Krogh [2] used the simplified geometry of a tissue cylinder around a centrally located capillary. Since then, several extensions have been made to this model to establish the basis of calculation of partial pressure of oxygen (pO_2) in muscle tissue [3].

While modeling of O_2 diffusion in the tissue is quite straightforward, the capillary release still poses considerable problems. In the literature,

it was mainly investigated by numerical methods for a limited number of capillaries and in simplified tissue situations. Since such numerical results cannot be easily incorporated into tissue models, we developed analytical methods [1, 3] that allow an estimation of the effect on pO_2 in various circumstances. The effect was quantified as an extraction pressure (EP; for a complete list of symbols used in this article, see Table 1), defined as follows. First, the O_2 driving pressure was calculated in the tissue at a point distant from the capillary via the homogeneous blood model. Then, the same was done at the same tissue location for the model with erythrocytes as distant O_2 sources. EP was the difference in predicted O_2 driving pressure between both models. When no myoglobin is active in the tissue, this O_2 driving pressure was equal to pO_2.

The model presented here is an extension of the two previous models [1, 3], that accounts for erythrocyte movement in the capillary. The model only considers equidistant erythrocytes all moving with the same speed. Results were again calculated in terms of EP, where it is most interesting now to look at the differences from former models.

2. THEORY

2.1. ASSUMPTIONS AND BASIC EQUATIONS

Diffusional transport of O_2 is considered in a cylindrical layout with coordinates (r, ϕ, z). The angle coordinate ϕ will be dropped because we assume cylindrical symmetry, so $\vec{r} = (r, z)$. Along the z axis, equidistant pointlike O_2 sources are located at distances Δz moving with velocity v in the direction of the axis (Figure 1). The point sources represent erythrocytes moving in a capillary of radius r_c. The consequences for tissue oxygenation will be primarily worked out in a concentric tissue cylinder of radius R so that each point source supplies a tissue volume $V = \pi R^2 \Delta z$. In Figure 1, such volumes are shown separated by circular cross-sections with the point sources as black dots in their centers. The origin of the z axis is chosen at one of these source locations so that the ith source is located at $\vec{r_i} = (0, z_i)$ where $z_i = i \Delta z$.

The O_2 transport equations in the tissue are for diffusion and mass balance. For diffusion of O_2:

$$\vec{J} = -\mathscr{P}\vec{\nabla}p \tag{1}$$

where $\vec{J}$ is oxygen flux, $\mathscr{P}$ is oxygen permeability of the tissue (product of oxygen diffusion coefficient D and oxygen solubility α) and p is O_2

TABLE 1

Symbols

Symbol	Meaning
A	O_2 supply area of one source in the r-plane
a_0, a_1	integration constants
a_C	level constant in $F_C(\ )$
a_T	level constant in $F_T(\ )$
b_{0n}, b_{1n}	coefficients in $f_{cn}(\ ), f_{sn}(\ )$
$CI_1 \cdots CI_6$	integration contours (Appendix A) in complex plane
c	concentration of oxygen
c_{0n}, c_{1n}	coefficients in $f_{cn}(\ ), f_{sn}(\ )$
D	diffusion coefficient of O_2 in tissue
EP	extraction pressure
exp(x)	e^x
F_{00}, F_{10}, F_{11}	constants in source contour description (Appendix C)
$F_1(\ )$	contour function for one source
$F_C(\ )$	source(s) term in continuous model
F_{EP}	dimensionless extraction pressure
F_R	dimensionless pO_2 drop across tissue cylinder
$F_{S,N}(\ )$	recalibrated source sum term in stroboscope solution
$F_{S,\infty}(\ )$	limit of $F_{S,N}(\ )$ for $N \to \infty$
$F_T(\ )$	moving-sources term in time-dependent solution
ΔF_T	dimensionless difference between continuous and time-dependent solution
$F_\varepsilon(\ )$	difference between $F_T(\ )$ and $F_{S,\infty}(\ )$
$f_{cn}(\ ), f_{sn}(\ )$	Fourier coefficient functions in $F_\varepsilon(\ )$
G_z	constant in contour integral
g_{01}	limit constant in contour integral
$g_n(\ ), g_n^*(\ )$	Fourier coefficient functions in $F_{S,\infty}(\ )$
Hct	capillary hematocrit
$I_0(\ )$	modified Bessel function of the first kind
$\Im m\langle\ \rangle$	imaginary part of a complex expression
i	$\sqrt{-1}$
$\vec{J}$	flux of O_2
$K_0(\ )$	modified Bessel function of the second kind
k, k'	reaction rates of myoglobin with O_2
ln( )	natural logarithm
Mb	myoglobin
N	indicating the number of sources (N or $2N + 1$)
O_2Mb	oxymyoglobin
$\mathscr{P}$	permeability of O_2 in tissue
p, pO_2	O_2 partial pressure
p^*	O_2 diffusion driving quantity
p_E	erythrocyte O_2 pressure
p_F	facilitation pressure
p_S	O_2 pressure as calculated from the stroboscope model
Q	O_2 consumption per tissue volume

TABLE 1 (*Continued*)

| Symbol	Meaning
R	radius of tissue cylinder
$\Re e\langle\ \rangle$.	real part of a complex expression
r	radial coordinate in cylindrical coordinate system
$\vec{r}$	coordinate vector
r_c	radius of capillary
r_E	radial coordinate value of boundary condition
r_{sE}	radius of spherical erythrocyte
$\vec{r}_i$	location of the ith source
s_E	distance of location on the source contour to the source itself
s_{Mb}	myoglobin saturation
t	time
u	integration variable in contour integral
V	volume consuming an amount of O_2 that can be supplied by one source
V_E	erythrocyte volume
v	velocity of sources along the z-axis
Z	arbitrary large number in contour integral
z	axial coordinate in cylindrical coordinate system
z'	axial coordinate in moving frame, $z' = z - vt$
z_0, z_1	axial limits of source contour, i.e., equivalent erythrocyte contour
z_E	axial coordinate value of boundary condition
z_i	axial coordinate of the ith source
Δz	distance between two successive sources
α	O_2 solubility in tissue
γ	angular variable in contour integral
δ	equal to $Z\sin(\varepsilon)$, small number approaching zero
ε	arbitrary small number in contour integral
ζ	integration variable in contour integral
$\lambda_n, \bar{\lambda}_n$	complex coefficient in Bessel series and its complex conjugate
ρ	radial value of source contour
$\Phi(\ )$	field term
ϕ	angular coordinate in cylindrical coordinate system
$\Psi_N(\ )$	field term for N sources in the stroboscope model
$\Psi_\infty(\ )$	limit of $\Psi_N(\ )$ for $N \to \infty$
ω	cyclic wavelength in Fourier expansion of the stroboscope model
$\cdot$	vector inner product
$\vec{\nabla}$	gradient operator
∇^2	Laplace operator
∇_r^2	radial part of Laplace operator in cylindrical coordinate system
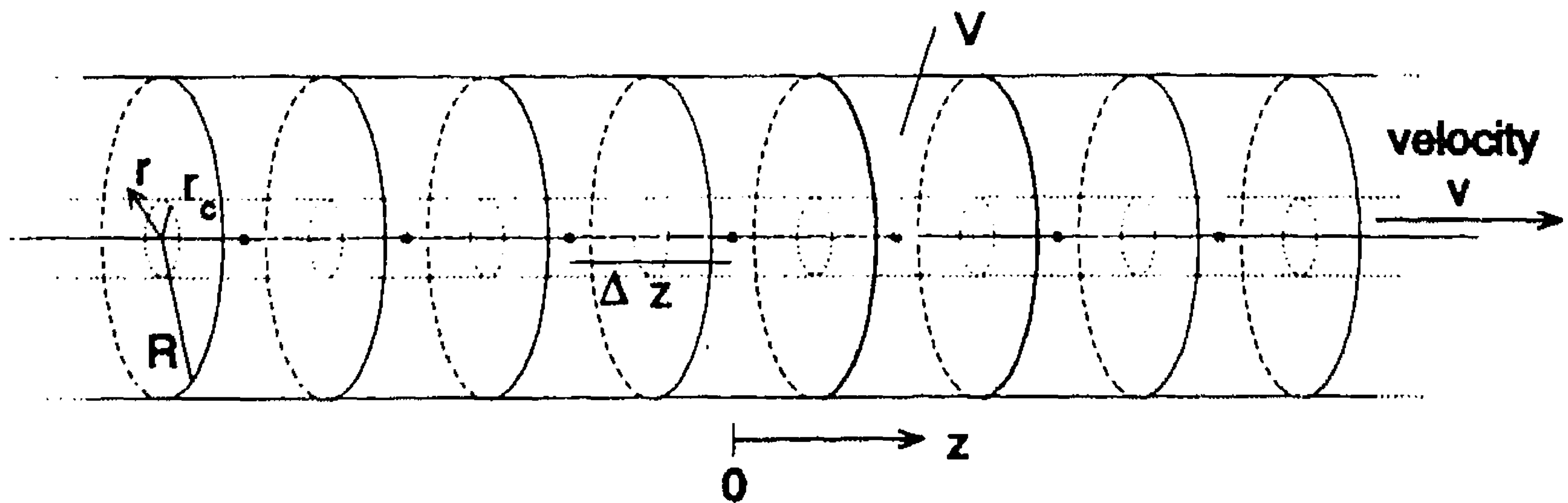
FIG. 1. Cylindrical coordinate system $\vec{r} = (r, z)$ with capillary of radius r_c containing pointlike O_2 sources (black dots) equidistant with spacing Δz all moving along the z-axis with constant velocity v. In a surrounding tissue cylinder of radius R, each source distributes its O_2 into an equal amount of tissue of volume V.

partial pressure. For mass balance of O_2:

$$\frac{\partial c}{\partial t} + \vec{\nabla} \cdot \vec{J} = -\dot{Q} \tag{2}$$

where c is O_2 concentration, $\dot{Q}$ is O_2 consumption per tissue volume, and the bold dot ($\cdot$) denotes vector inner product. The concentration is proportional to pressure according to Henry's law:

$$c = \alpha p \tag{3}$$

These equations have to be extended when there is myoglobin (Mb) present in the tissue since this species can bind and release O_2 at a certain rate and also transport it through diffusion of the O_2Mb complex. As these aspects make the description much more complicated, we assume here that either there is no Mb or that its contribution to O_2 transport is negligible, which will be discussed later.

2.2. SOLUTIONS

In a previous article [1], we used a stroboscope technique to construct an analytical solution for O_2 diffusion into the tissue. With this technique, the erythrocytes were considered only at specific time intervals when each erythrocyte had moved to the exact position where its predecessor was formerly. Also with this technique, Mb can be incorpo-

rated, and a solution was found in terms of an equivalent p^* driving the O_2 diffusion:

$$p^* = \frac{\dot{Q}}{4\mathscr{D}}\left\{\Phi(\vec{r}) + \sum_{i=1}^{N}\frac{V}{\pi|\vec{r}-\vec{r}_i|}\right\} \tag{4}$$

where $\Phi(\vec{r})$ was a function called the *field term* of dimension r^2, and the sources were numbered from 1 to N in a cylinder of limited length. The O_2 driving pressure p^* is equal to $p + p_F S_{Mb}$, where s_{Mb} is Mb saturation and p_F is the so-called facilitation pressure, quantifying the maximum effect of Mb on O_2 transport [3]. Here, without Mb, p^* is equal to the O_2 pressure p. The field term $\Phi(\vec{r})$ was a smooth solution of $\nabla^2\Phi = 4$, depending on tissue geometry but not on the individual sources whose contribution was accounted for in each of the sum terms. In the geometry here, the sources extend in both directions and are counted as $i: -N \to N$. For a moving-sources solution, we have to consider the case where $N \to \infty$. However, since the individual sum terms in (4) are of order i^{-1}, they do not approach zero fast enough for the summation to converge. This can be corrected by the following redefinition of (4), also using $V = \pi R^2 \Delta z$:

$$p_S = \frac{\dot{Q}}{4\mathscr{D}}\left\{\Psi_N(\vec{r}) + R^2 F_{S,N}(\vec{r})\right\} \tag{5}$$

where

$$\Psi_N(\vec{r}) = \Phi(\vec{r}) + \sum_{i=-N}^{N}\frac{\Delta z}{\sqrt{r_c^2 + z_i^2}} \tag{6}$$

$$F_{S,N}(\vec{r}) = F_{S,N}(r,z) = \sum_{i=-N}^{N}\left(\frac{\Delta z}{|\vec{r}-\vec{r}_i|} - \frac{\Delta z}{\sqrt{r_c^2 + z_i^2}}\right) \tag{7}$$

and the subscript S now denotes that this solution comes from the stroboscope approach; $\Psi_N(\vec{r})$ is the corresponding new field term for $2N + 1$ sources. Note that it is still smooth since only constant terms are added to $\Phi(\vec{r})$. Furthermore, $F_{S,N}(r_c, 0) = 0$ and the function is dimensionless. This formulation can be extended to an infinite number of sources since the terms in the summation now approach order i^{-2}. For $N \to \infty$ the erythrocyte contribution can be written in terms of a Fourier series, an approach that has also been tried earlier [3]; it can be derived

that a representation is possible in terms of the modified Bessel function $K_0(\ )$ (see Appendix A):

$$F_{S,x}(r,z) = \sum_{n=1}^{\infty} 4\{K_0(n\omega r)\cos(n\omega z) - K_0(n\omega r_c)\} - \ln\left(\frac{r^2}{r_c^2}\right) \quad (8)$$

where $\omega = 2\pi/\Delta z$. This sum is finite since $K_0(\ )$ quickly approaches zero when its argument grows large.

The above equations can be used as a basis for deriving the full time-dependent solution:

$$p = \frac{Q}{4\mathscr{P}}\{\Psi_\infty(\vec{r}) + R^2 F_T(r,z,t)\} \quad (9)$$

where $F_T(r, z, t)$ is the assembled moving-sources term. As a basis for solving $F_T(\ )$ we can use $F_{S,\infty}(r, z - vt)$, which is also a moving-sources function but does not obey (2). The difference between the two functions is called $F_\varepsilon(r, z, t)$:

$$F_\varepsilon(r,z,t) = F_T(r,z,t) - F_{S,\infty}(r,z-vt) \quad (10)$$

Since $F_T(\ )$ describes the infinite number of moving sources, it is stationary and periodic in a moving frame $z' = z - vt$. Therefore we can express $F_T(\ )$ and $F_\varepsilon(\ )$ in terms of a Fourier series:

$$F_\varepsilon(r,z,t) = \sum_{n=0}^{\infty} \{f_{cn}(r)\cos(n\omega[z-vt]) + f_{sn}(r)\sin(n\omega[z-vt])\}$$

$$\quad (11)$$

As for $\Phi(\ )$, $\nabla^2\Psi_\infty = 4$ and we can substitute (1), (3), (9), and (10) into the time-dependent differential equation (2) to derive

$$\left(\nabla^2 - \frac{1}{D}\frac{\partial}{\partial t}\right)\{F_{S,\infty}(r,z-vt) + F_\varepsilon(r,z,t)\} = 0 \quad (12)$$

where $\mathscr{P} = \alpha D$ is also substituted. Then, inserting (8) and (11) leads to

$$-\frac{v}{D}\sum_{n=1}^{\infty} 4n\omega K_0(n\omega r)\sin(n\omega z')$$

$$+\sum_{n=0}^{\infty}\left[\left\{(\nabla_r^2 - n^2\omega^2)f_{cn}(r) + \frac{n\omega v}{D}f_{sn}(r)\right\}\cos(n\omega z')\right.$$

$$\left. +\left\{(\nabla_r^2 - n^2\omega^2)f_{sn}(r) - \frac{n\omega v}{D}f_{cn}(r)\right\}\sin(n\omega z')\right] = 0 \quad (13)$$

where ∇_r^2 is the r-dependent part of the Laplace operator and $z' = z - vt$. The solutions for the coefficient functions $f(\ )$ are (see Appendix B):

$$f_{c0}(r) = a_0 \tag{14}$$

$$f_{cn}(r) = 2K_0(\lambda_n r) + 2K_0(\bar{\lambda}_n r) - 4K_0(n\omega r) \qquad n \geqslant 1 \tag{15}$$

$$f_{sn}(r) = 2iK_0(\lambda_n r) + 2iK_0(\bar{\lambda}_n r) \qquad n \geqslant 1 \tag{16}$$

with an integration constant a_0 and complex values (including $i = \sqrt{-1}$) for λ_n and its complex conjugate $\bar{\lambda}_n$:

$$\lambda_n = \sqrt{(1/2)n\omega\left\{\sqrt{n^2\omega^2 + (v/D)^2} + n\omega\right\}}$$

$$+ i\sqrt{(1/2)n\omega\left\{\sqrt{n^2\omega^2 + (v/D)^2} - n\omega\right\}} \tag{17}$$

Note that $1/2\{K_0(\lambda_n r) + K_0(\bar{\lambda}_n r)\} = \Re e\langle K_0(\lambda_n r)\rangle$ is the real part and $-(1/2)i\{K_0(\lambda_n r) - K_0(\bar{\lambda}_n r)\} = \Im m\langle K_0(\lambda_n r)\rangle$ is the imaginary part of the Bessel function. The value of the constant a_0 must follow from the boundary conditions, which is considered below. The above treatment can be gathered into a single expression for $F_T(\ )$:

$$F_T(r,z,t) = \sum_{n=1}^{\infty} \llbracket 2\{K_0(\lambda_n r) + K_0(\bar{\lambda}_n r)\}\cos(n\omega[z - vt])$$

$$- 2i\{K_0(\lambda_n r) - K_0(\bar{\lambda}_n r)\}\sin(n\omega[z - vt])\rrbracket + a_T - \ln\left(\frac{r^2}{r_c^2}\right) \tag{18}$$

where a_T is a constant again, or, simplified:

$$F_T(r,z,t) = 4\sum_{n=1}^{\infty} \Re e\langle K_0(\lambda_n r)\exp(-in\omega[z - vt])\rangle + a_T - \ln\left(\frac{r^2}{r_c^2}\right) \tag{19}$$

where again $\Re e\langle\ \rangle$ means the real part of the respective complex equation. It is easily seen that for $v/D \to 0: \lambda_n \to n\omega$ (no imaginary part) and consequently $F_T(r, z, t) \to F_{S,\infty}(r, z - vt)$. So the stroboscope method emerges here as the limit for zero velocity as should be the case, which is discussed below.

2.3. REPRESENTATION

The important effect of the particulate nature of blood is that the calculated pO_2 with this model is lower than with the homogeneous blood model. The resulting difference can be quantified as **EP** [1, 3], which is the extra pressure drop resulting "far away" from the capillary. Let us denote the function equivalent to $F_T(\ )$ for continuous nonparticular blood as $F_C(\ )$; an expression for this function can be derived as the limit of $F_T(\ )$ for $\Delta z \to 0$, that is, approaching zero spacing between the sources while maintaining O_2 delivery the same. This means $\omega \to \infty$ so $\lambda_n \to \infty$ and thus all $K_0(\ ) \to 0$ in (18) or (19) so that

$$F_C(r,z,t) = a_C - \ln\left(\frac{r^2}{r_c^2}\right) \qquad (20)$$

Obviously, this function no longer depends on z and t as it makes no difference whether a continuous line of sources is moving or non-moving. Note that the tissue z-dependency has been accounted for in the field term $\Psi_z(\ )$. Now it can be seen easily that all three functions $F_{S,z}(\ )$, $F_T(\ )$, and $F_C(\ )$ approach the same functional behavior for large r (i.e., far away from the capillary) except for a difference in level resulting from the values of a_T and a_C. It is this difference in level that determines **EP**; the absolute level of tissue O_2 pressure is irrelevant when there is no Mb present or active. For the continuous phase, **EP** by definition is zero. So, relevant here is the functional difference $F_T(\ ) - F_C(\ )$. Instead of evaluating the value of this difference for large r, we subtract the limit value defining

$$\Delta F_T(\ ) = F_T(\ ) - F_C(\ ) - \lim_{r \to \infty} \{F_T(\ ) - F_C(\ )\} \qquad (21)$$

which can be evaluated by use of (18) and (20):

$$\Delta F_T(r,z') = \sum_{n=1}^{\infty} [\![2\{K_0(\lambda_n r) + K_0(\bar{\lambda}_n r)\}\cos(n\omega z')$$

$$- 2i\{K_0(\lambda_n r) - K_0(\bar{\lambda}_n r)\}\sin(n\omega z')]\!] \qquad (22)$$

Note that $z' = z - vt$. This dimensionless function is plotted and used to evaluate **EP**. The evaluation is done for $t = 0$ for the erythrocyte at $z = 0$. By definition, **EP** is the limiting difference between p of (9) and

the equivalent equation with $F_C(\ )$ instead of $F_T(\ )$ evaluated at large distance:

$$\text{EP} = \frac{\dot{Q}R^2}{4\mathscr{P}} \lim_{r \to \infty} \{F_C(r,0,0) - F_T(r,0,0)\} = \frac{\dot{Q}R^2}{4\mathscr{P}} \{a_C - a_T\} \quad (23)$$

where for the righthand part (18) and (2) have been substituted. The boundary condition is that erythrocyte pressure p_E must be reached at the erythrocyte border, which was an equivalent sphere radius r_{sE} for the stroboscope model [1]. For the present model, this location is denoted by (r_E, z_E); for the continuous model, it is the capillary border $(r_c,0)$. These locations have to be inserted into the respective equations, (r_E,z_E) in (9) and $(r_c,0)$ into its limit for $\Delta z \to 0$, which is the same equation (9) in which $F_T(\ )$ has been replaced by $F_C(\ )$ from (20). This leads to

$$\frac{4\mathscr{P}p_E}{\dot{Q}} = \Psi_\infty(r_E,z_E) + R^2 F_T(r_E,z_E,0) = \Psi_\infty(r_c,0) + R^2 F_C(r_c,0,0)$$

$$(24)$$

where (r_E,z_E) can be obtained from the implicit set of equations (see Appendix C):

$$V_E = \frac{4}{3}\pi r_{sE}^3 = \pi z_1^2 \left(\frac{\exp\{2(v/D)z_1\}-1}{v/D} - \frac{2}{3}z_1 \right) \quad (25)$$

$$\ln(-z_0) = \ln(z_1) + (v/D)z_1 = \ln(s_E) + \frac{(v/D)s_E}{2+(v/D)s_E} \quad (26)$$

$$(r_E,z_E) = \frac{s_E}{2+(v/D)s_E}\left(2\sqrt{1+(v/D)s_E}, -(v/D)s_E \right) \quad (27)$$

where V_E is the erythrocyte volume. We neglect the small differences between $\Psi_\infty(r_E,z_E)$ and $\Psi_\infty(r_c,0)$; note that $\Psi_\infty(\ )$ was a smooth function and that the respective distances are small. Then, approximately, according to (24):

$$F_T(r_E,z_E,0) = F_C(r_c,0,0) \quad (28)$$

For the lefthand term, we combine (18) and (22), and for the righthand term we use (20) to obtain

$$\Delta F_T(r_E, z_E) + a_T + \ln\left(\frac{r_E^2}{r_c^2}\right) = a_C, \qquad (29)$$

and substitution into (23) leads to

$$\mathbf{EP} = \frac{\dot{Q}R^2}{4\mathscr{P}} F_{\mathrm{EP}} \qquad (30)$$

$$F_{\mathrm{EP}} = \Delta F_T(r_E, z_E) - \ln\left(\frac{r_E^2}{r_c^2}\right) \qquad (31)$$

where (30) defines the dimensionless **EP**, F_{EP}.

3. RESULTS FOR RAT HEART

For calculation of results in terms of ΔF_T, values have to be known for $\Delta z, r_c, v/D$, and V_E. When **EP** is also involved, the value of $\dot{Q}R^2/(4\mathscr{P})$ has to be known. For rat heart, we use $r_c = 2.4$ μm [4] and $\dot{Q}/(4\mathscr{P}) = 0.00633$ kPa/μm^2 [5]. From the latter publication, the value $\alpha F/\mathscr{P} = 10.56$ μm is also used, where F is blood flow, to obtain $v/D = (\alpha F/\mathscr{P})/(\pi r_c^2) = 0.583$ μm^{-1} for normal flow. Since the effect of flow is investigated here, values of v/D of twice and five times this basic value (1.167 and 2.917 μm^{-1}) were also used, as well as $v/D = 0$, since this value yields the results of the stroboscope approach. For V_E, a value of 61 (μm)^3 was taken from Altman et al. [6] that is equivalent to a sphere radius $r_{sE} = 2.44$ μm. Source spacing Δz can be calculated from hematocrit (Hct) since Hct $= V_E/(\pi r_c^2 \Delta z)$, which for Hct values between 20% and 50% leads to spacings ranging from 16.9 μm to 6.7 μm.

Figure 2 shows profiles of ΔF_T for $\Delta z = 16.9$ μm (Hct = 20%) and for $v/D = 0$, 0.583, 1.167, and 2.917 μm^{-1}. The profiles of $\Delta F_T(\ )$ show the differences from the continuous-line-source model. These differences fade out quite quickly away from the capillary (increasing r). The profiles are restricted to $r > r_c$ and so are outside the capillary. While the gradients in ΔF_T are alternately positive and negative, the logarithmic terms of (20) have to be added for the actual O_2 pressure profiles. The resulting O_2 gradient is always away from the capillary (outward flux). The oscillatory profiles in Figure 2 then imply that flux to the surrounding tissue is higher close to the sources and lower in
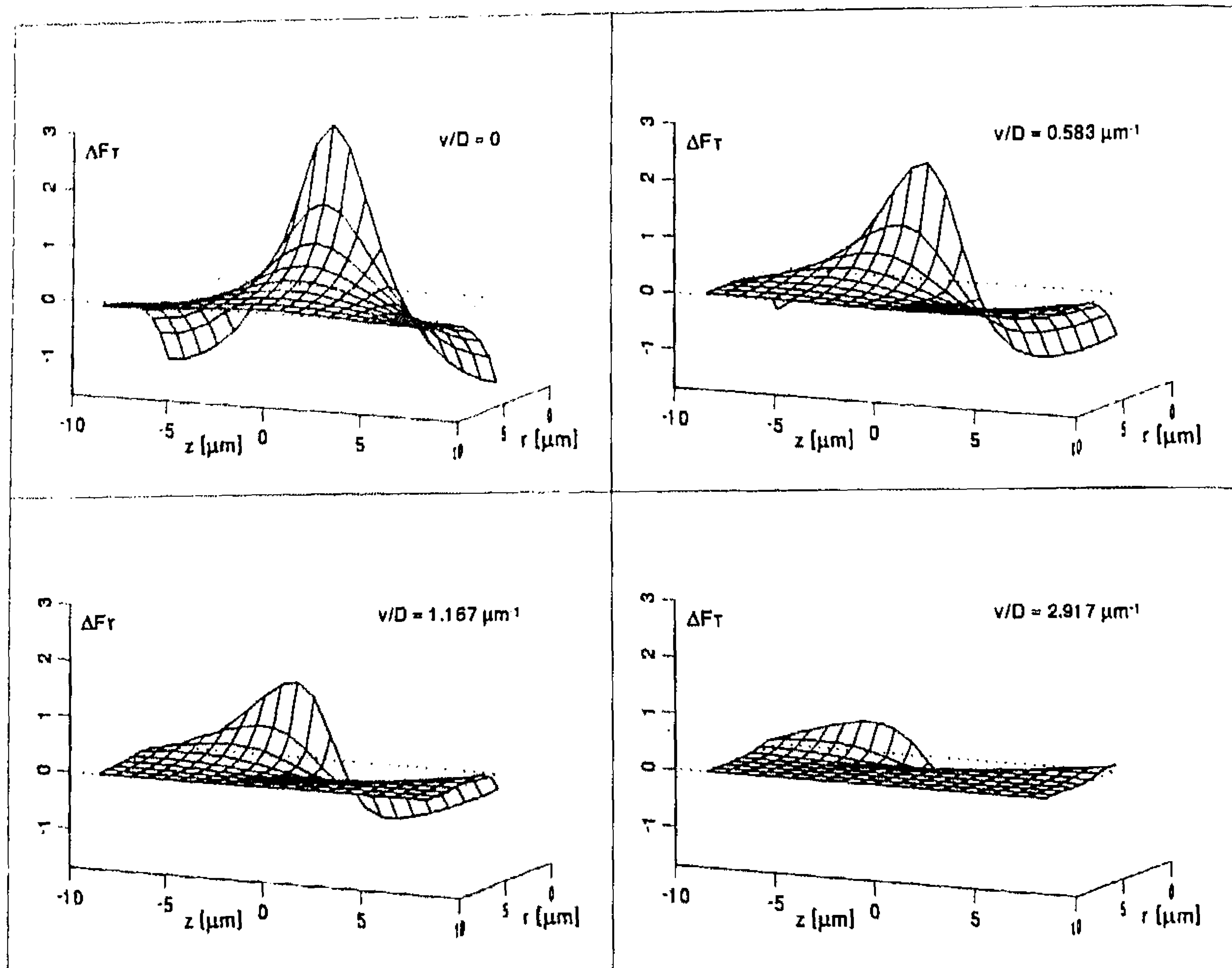
FIG. 2. Profiles of dimensionless difference function ΔF_T (solid lines) against coordinates (r, z) for source spacing $\Delta z = 16.9$ μm $(-8.45$ μm $< z < 8.45$ μm) outside the capillary $(r > r_c = 2.4$ μm) up to $r = 10$ μm as indicated by the dotted rectangle at level $\Delta F_T = 0$. Top left, stroboscope model $(v/D = 0)$; for the other panels, erythrocyte velocity as indicated in terms of v/D.

between. The profile for $v/D = 0$ is symmetric around the top value at $z = 0$. The other profiles are not symmetrical and are shifted toward negative z-values, while the source is still located at $(r, z) = (0, 0)$. Mathematically, this is due to the nonzero function coefficients of the $\sin(n\omega[z - vt])$ terms in (18). So, the O_2 field is "dragged behind" the moving source.

This is even clearer in Figure 3, where ΔF_T is plotted at $r = r_c$ for the full range of v/D values at low hematocrit (spacing $\Delta z = 16.9$ μm). For increasing velocity, the profile is shifted further toward negative values of z. Also, its size and shape change. The solid line is for high hematocrit (spacing $\Delta z = 6.7$ μm) at normal velocity and is added for comparison; it encompasses three sources instead of one. The symbols indicate the resulting EP in kPa (rightmost axis) for a cylinder with radius $R = 10$ μm $(QR^2/(4\mathscr{P}) = 0.633$ kPa), which is close to the average value for rat heart [4]. For a somewhat larger radius of $R = 12.6$
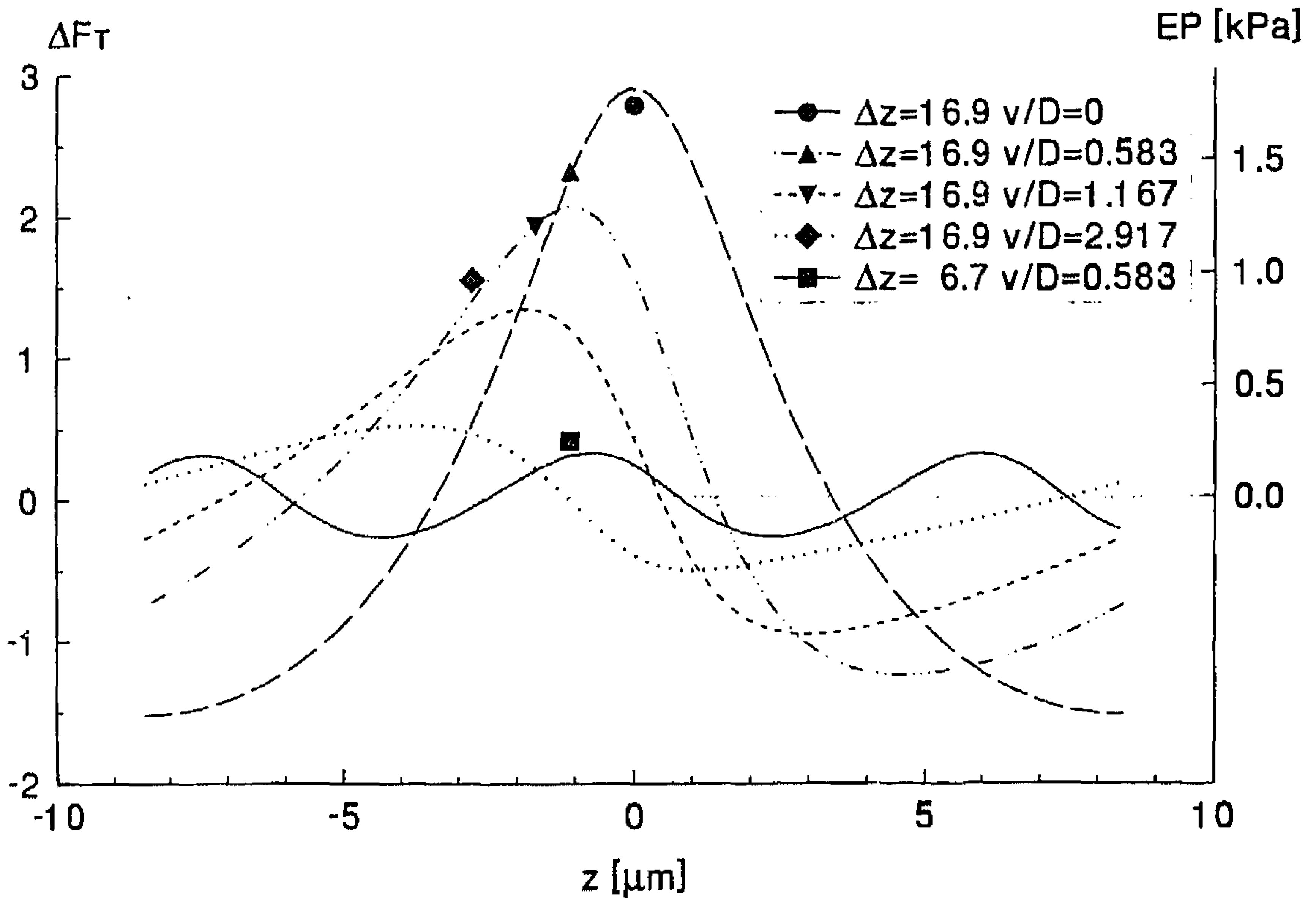
FIG. 3. Dimensionless difference function ΔF_T (left axis) along the capillary border ($r = r_c = 2.4$ μm; lines) against axial distance z for different values of spacing Δz and velocity v as indicated in the figure; Δz is in micrometers and v/D in micrometers^{-1}. The solid line encompasses three sources (at -6.7, 0, and 6.7 μm). Symbols represent resulting EP for a cylinder of radius $R = 10$ μm (right axis).

μm, the value of $\dot{Q}R^2/(4\mathscr{P})$ is 1.0 kPa, and the values of EP equal F_{EP} and can be read in kPa on the leftmost axis. A radius of 12.6 μm is quite possible, being $(3/2)\log$SD above the median value [4]. The EP is calculated from (30) and (31) on location (r_E, z_E) instead of $r = r_c$.

The locations (r_E, z_E) where EP is found are obtained from (25)–(27). The values calculated from these equations are listed in Table 2. Note that z_0 and z_1 are the tail and head of the equivalent erythrocyte contour (see Appendix C), and that the contour trails behind the source more and more, as its "center" $(1/2)(z_0 + z_1) < 0$. The "thickness" r_E, the most distance location from the source-line axis, decreases, which implies that the contour becomes more and more elongated.

The EP calculated for all the cases covered here are shown in Figure 4 as dimensionless EP, F_{EP}, calculated from (30), against source spacing Δz where the corresponding Hct values are shown on the upper horizontal axis. The values of v/D are listed in the figure. For normal blood velocity, $v/D = 0.583$ μm^{-1}, the results are not very different from those of the stroboscope model ($v/D = 0$). The differences increase for increasing velocity, and what is remarkable is that this implies

TABLE 2

Equivalent Erythrocyte Boundary Values [see (25)–(27)] for an Erythrocyte
Located at $(r, z) = (0,0)$ with Volume $V_E = 61$ $(\mu m)^3$ and for
Different Values of v/D

v/D $(\mu m)^{-1}$	s_E	r_E	z_E	z_0	z_1	$(1/2)(z_0 + z_1)$
			μm			
0	2.44	2.44	0	−2.44	2.44	0
0.583	2.55	2.31	−1.09	−3.91	1.57	−1.17
1.167	2.73	2.16	−1.68	−5.06	1.22	−1.92
2.917	3.33	1.86	−2.76	−7.63	0.78	−3.42

a decrease at low and an increase at high Hct. Recollect that F_{EP} equals EP in kPa for cylinder radius $R = 12.6$ μm and that EP $= 0.633 F_{EP}$ for $R = 10$ μm.

The values of F_{EP} can be compared with the pO_2 drop farther into the tissue in a cylinder model as laid out in Figure 1. For the classical
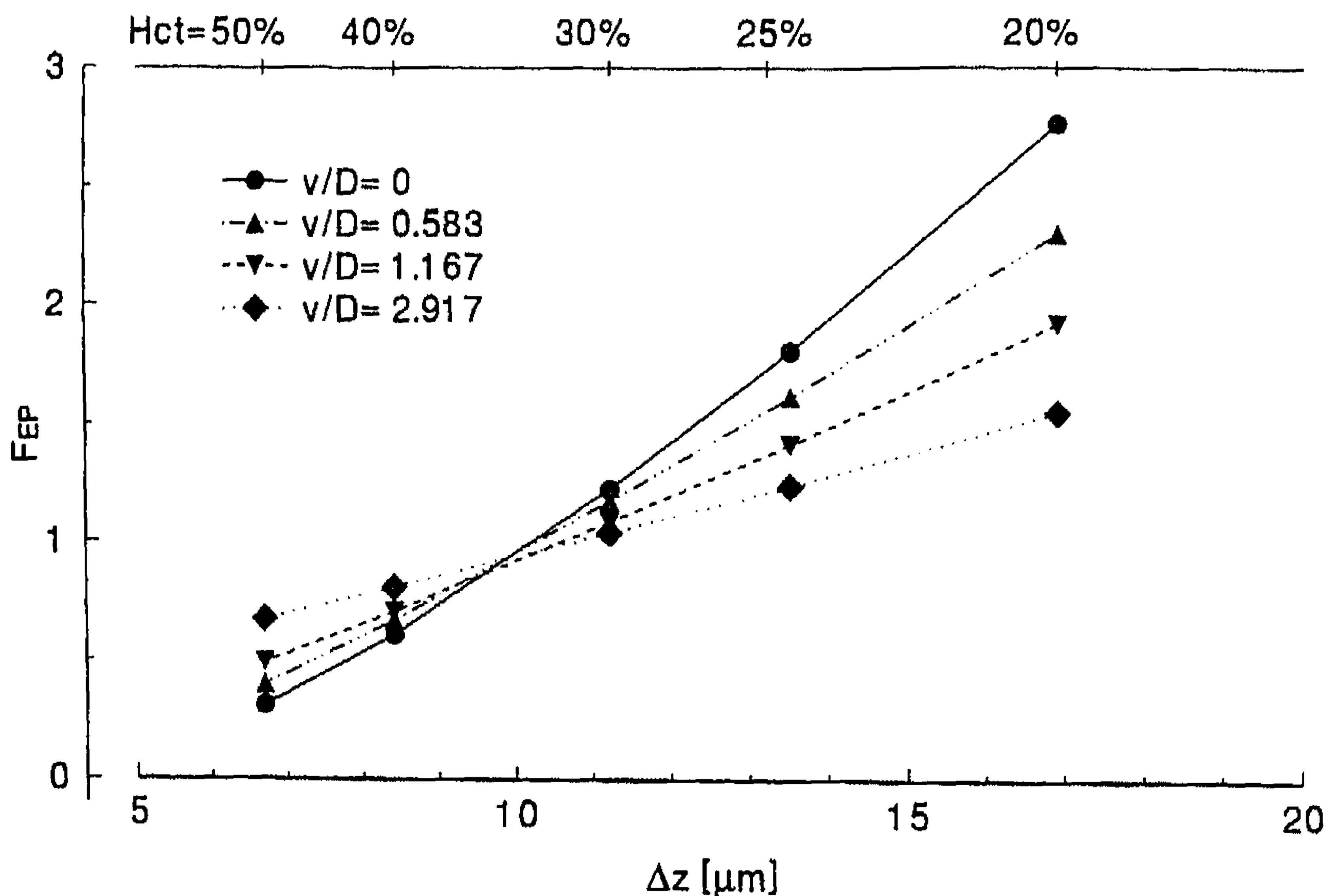

FIG. 4. Dimensionless extraction pressure (F_{EP}) against source spacing Δz for different source velocities as indicated in the figure; v/D is in micrometers^{-1}. On the upper horizontal axis the corresponding Hct values are shown. Values on the left axis equal EP in kilopascals for a cylinder radius of $R = 12.6$ μm.

Krogh model, a solution of this case for homogeneous blood [2], we have in (9):

$$\Psi_{\infty}(\vec{r}) \Rightarrow \frac{4\mathscr{P}p_E}{Q} - R^2 a_C + r^2 - r_c^2 \tag{32}$$

and $F_T(\ )$ replaced by the $F_C(\ )$ of (20). From this, we calculate an equivalent dimensionless value for the pO_2 drop from capillary to cylinder border as

$$F_R = \left\{ R^{-2}\Psi_{\infty}(r_c) + F_C(r_c) \right\} - \left\{ R^{-2}\Psi_{\infty}(R) + F_C(R) \right\}$$

$$= \ln\left(\frac{R^2}{r_c^2}\right) - 1 + \frac{r_c^2}{R^2} \tag{33}$$

This dimensionless tissue pO_2 drop $F_R = 1.91$ for the typical cylinder radius $R = 10$ μm. For low Hct, F_{EP} is of comparable size or even larger. So, in those cases pO_2 drop around the erythrocyte is more important than the pO_2 drop further on into the tissue. For the larger $R = 12.6$ μm, (33) yields $F_R = 2.35$, so that the tissue pO_2 drop is more important. However, the low-velocity low-Hct F_{EP} is still larger.

4. DISCUSSION

The moving-sources model presented here is an extension of the stroboscope model [1]. First, the stroboscope model is extended to an infinite number of sources, leading to the alternative mathematical formulation of (5) and (8). Then, the effect of movement v/D is added, resulting in (18) or (19). The improvements are that effects of erythrocyte movement are incorporated, and also that the solution is largely independent of the tissue model since most of the calculations, up to and including the dimensionless EP F_{EP}, can be done without using the cylinder radius R. The remaining prerequisite is that all sources are equal, each distributing an equal amount of O_2 to supply a volume V. So, results are likely to be of more general validity than for a tissue cylinder only. The disadvantages are that no effects of Mb are incorporated, and calculations are more complicated, involving complex modified Bessel functions. Note that the stroboscope model was capable of incorporating effects of Mb.

This model defaults to the stroboscope model in the limit for $v/D \rightarrow 0$, or, more correctly, to the stroboscope model extended to an infinite number of sources. This can be best judged from (12), where for $v = 0$ $F_{S,\infty}(r, z)$ already obeys the equation, without any $F_c(r, z, t)$ needed.

The stroboscope model predicted results for EP virtually independent of Mb concentration [1]. So, from analogy with this former model,

it is to be expected that these results will be valid for Mb-containing tissue as long as the myoglobin is not functional near the capillary. This might often be a valid assumption [3]. When Mb functions close to the capillary, the oscillations in pO_2 would generate oscillations in oxymyoglobin. In such oscillations, diffusion of Mb itself (with a much lower diffusion coefficient than O_2), as well as its O_2 reaction rates k and k', plays a role. This makes a full theoretical treatment substantially more complicated.

The importance of **EP** as predicted by earlier models [1, 3] is confirmed also for moving erythrocytes, as seen best in Figure 4. The influence of moving sources on the mathematical model shows itself as an enhancement of transport in the z-direction; the Laplacian ∇^2 of the diffusion equation is replaced by an effective term $\nabla^2 + (v/D)\partial/\partial z$, as can be deduced from (12). Compared with the stroboscope model, this means that profiles in the z-direction are smoothed. The symbols in Figure 3 represent the erythrocyte value p_E, and the higher values within the equivalent erythrocyte contour decrease, whereas the lower values in between the contours increase. For large source distances Δz, the increased portion is larger than the decreased portion, and the average level is increased, leading to a lower value of **EP**. For small Δz the opposite is true, and **EP** is increased. In Figure 4, a crossover point can be seen located around 35% Hct, that is, $4r_{sE}$ (9.77 μm), where for the sphere contour the gap spacing is equal to the contour length.

The pO_2 smoothing effect shows itself in the elongated equivalent erythrocyte contour. The z-transport is increased at the expense of r-transport. The thickness r_E decreases from 2.44 μm to 1.86 μm, as seen from Table 2. O_2 release starts from the location (r_E, z_E) where pO_2 equals p_E. For decreasing r_E, this location is more remote from the tissue, which has a marked effect on **EP** as can be seen from the difference between the symbols and their corresponding lines in Figure 3. Due to this increased delivery distance, **EP** would always be increased were it not that this is counteracted by the increased z-transport, most effectively for large Δz.

On the other hand, the increase of **EP** with v/D at high Hct (source spacing $\Delta z < 10$ μm) would possibly not be as pronounced as calculated here. The present model is an assembled point-sources model, and consequently the (r_E, z_E) are calculated for isolated sources. When the sources are close together this is no longer valid; from Table 2 it can be seen that the most elongated contours even overlap for small spacings Δz. In fact, it is no longer possible to find a contour where O_2 pressure has a fixed value p_E. This means that r_E effectively is larger (less elongated contour) and consequently **EP** is lower, so that the crossover point shifts toward lower Δz. The finite dimensions of the erythrocyte

also might contribute to an effectively lower EP here. However, EP is less important for high Hct; the most significant values for EP are not for small but for large spacing.

Akmal et al. [7] probably were the first to show the difference between erythrocyte and plasma pO_2 in a moving-erythrocytes model (Figure 3 of their publication). They numerically calculated a regular multicapillary model of skeletal muscle. They did not quantify the effect of erythrocyte spacing or erythrocyte movement on tissue pO_2. Groebe and Thews [8] numerically solved a moving-erythrocytes model in and closely around the capillary for maximally working skeletal muscle and for boundary conditions of either constant pO_2 or constant O_2 flux. When considering these as limiting cases, they concluded that erythrocyte movement increased tissue pO_2. Their explanation was that each erythrocyte coming by causes an O_2 burst into the tissue, thus raising local pO_2 impeding the flux out of the following plasma. Effectively, this would mean more O_2 flux in the z-direction. So this argument agrees with our reasoning. These "bursts" and "impediments" of radial O_2 flux can be seen in our Figure 2 as the waves of negative and positive radial slopes of the ΔF_T profile.

The results for rat heart show that EP can be very important. Whereas Hct values in larger blood vessels are $\sim 40\%$, the values detected in capillaries can be much lower [9]. At Hct = 20%, the pericapillary pO_2 drop—within a few micrometers—is larger than for the rest of the tissue—over 10 μm—thus leading to steep pericapillary pO_2 gradients. The amount of O_2 delivered to the capillary is determined by the product of Hct and flow, so the low-Hct capillary has normal O_2 supply for a doubled flow. But the extraction pressures for the respective situations Hct = 40%, $v/D = 0.583$ μm^{-1} and Hct = 20%, $v/D = 1.167$ μm^{-1} are quite different; see Figure 4. This leads to the conclusion that the O_2 delivery, defined as the product of blood oxyhemoglobin concentration and blood flow (mol/sec), cannot be the single primary determinant of tissue oxygenation. It is sometimes argued that high blood velocity might hamper O_2 distribution into the tissue, since there would be no time for the O_2 to be released. It is shown here, however, that the opposite is true, especially at low Hct.

Tsai and Intaglietta [10, 11] numerically solved a moving-erythrocytes model in a Krogh cylinder with pO_2-dependent O_2 consumption. They did not make quite clear how they numerically handled erythrocyte velocity and did not analyze its effect on tissue pO_2, but they demonstrated a clear effect of velocity on oxygenation of the whole tissue cylinder under conditions of equal O_2 supply to the capillary. Also their Figure 5 [10] nicely shows the elongation of the pO_2 profiles around the sources.

The dimensionless EP F_{EP} as defined in (30) is independent of actual O_2 delivery and therefore seems more adequate for incorporation into tissue models. Revising the definition, the relationship between EP and F_{EP} could be generalized as

$$EP = \frac{\dot{Q}A}{4\pi\mathscr{P}} F_{EP} \qquad (34)$$

where A is the O_2 supply area of the source, equal to πR^2 in the tissue cylinder model. Incorporation into tissue models is quite possible [3], the more so since individual calculations generally take less than a second (on an IBM PS2, 16 MHz), and the resulting F_{EP} is valid for an entire capillary, given the assumption of equally spaced erythrocytes.

With the presentation of the stroboscope model [1], it was argued that the model would be approximately valid for two regimes, low and high Δz. The low-Δz regime was expected for low Peclet numbers $v\Delta z/D$, but this is unrealistic because Δz would have to be lower than even for packed erythrocytes (Hct = 100%). The high-Δz regime was expected for $\Delta z^2 \gg 14.7(v/D)r_c^3$. This suggests a better validity for low v/D. It is true indeed that the results of both models diverge for increasing v/D (see Figure 4) and that the models match for $v/D = 0$. For $v/D = 0.583$ μm^{-1} we calculate $\Delta z^2 \gg (10.8 \ \mu$m$)^2$ for the inequality. The largest value of Δz here is 16.9 μm, which is of comparable size and so would not be expected to fulfill the inequality. Indeed, from the figure no approach can be seen toward the stroboscope calculation for increasing Δz. However, for normal velocity the deviations are not large, and the stroboscope model might serve as a sufficient first approximation. Its results can be calculated much more easily than those of the model discussed here.

In conclusion, the moving-sources model presented here seems valuable, predicting quite meaningful results for the rat heart. Even in that tissue, with its relatively small capillary distances, EP of several kilopascals can be present, adding a significant extra pO_2 drop in the O_2 transport cascade.

APPENDIX A: FOURIER EXPANSION OF SOURCE SERIES

Since $F_{S,N}(r, z)$ is periodic with spacing Δz and also is symmetric in z, the Fourier series for $F_{S,\infty}(\ )$ can be expressed in terms of cosine functions only:

$$F_{S,\infty}(r, z) = \sum_{n=0}^{\infty} g_n(r)\cos(n\omega z) \qquad (A1)$$

where $\omega = 2\pi/\Delta z$ and the Fourier coefficients $g_n(r)$ follow from integration over $-(1/2)\Delta z \rightarrow +(1/2)\Delta z$. These are calculated separately for $n = 0$ and for $n > 0$; for the latter terms, so for $n \geqslant 1$:

$$g_n(r) = \frac{2}{\Delta z} \int_{-1/2\Delta z}^{1/2\Delta z} dz'' F_{S,\infty}(r,z'')\cos(n\omega z'') \qquad (A2)$$

where z'' is the integration variable. When substituting the limit $(N \rightarrow \infty)$ of (7) for $F_{S,\infty}(r,z)$ and $\vec{r}_i = (0, z_i) = (0, i\Delta z)$ we derive

$$g_n(r) = \int_{-1/2\Delta z}^{1/2\Delta z} dz'' \lim_{N \rightarrow \infty} \sum_{i=-N}^{N}$$

$$\times \left[\frac{2}{\sqrt{r^2 + (z'' - i\Delta z)^2}} - \frac{2}{\sqrt{r_c^2 + (i\Delta z)^2}} \right]\cos(n\omega z'') \qquad (A3)$$

The next step is to interchange the limit and summation with the integration, which is allowed because the sum terms decrease fast enough:

$$g_n(r) = \lim_{N \rightarrow \infty} \sum_{i=-N}^{N} \left[\int_{-1/2\Delta z}^{1/2\Delta z} dz'' \frac{2}{\sqrt{r^2 + (z'' - i\Delta z)^2}} \cos(n\omega z'') \right.$$

$$\left. - \int_{-1/2\Delta z}^{1/2\Delta z} dz'' \frac{2}{\sqrt{r_c^2 + (i\Delta z)^2}} \cos(n\omega z'') \right] \qquad (A4)$$

Then for each term of the summation the rightmost integral yields zero because it is a constant integrated over a cosine, whereas for the leftmost integral we define a new integration variable $\zeta = z'' - i\Delta z$ so that

$$g_n(r) = \lim_{N \rightarrow \infty} \sum_{i=-N}^{N} \left[\int_{(-i-(1/2)\Delta z)}^{(-i+(1/2)\Delta z)} d\zeta \frac{2}{\sqrt{r^2 + \zeta^2}} \cos(n\omega\zeta) \right] \qquad (A5)$$

which, through the substitution $Z = (N + 1/2)\Delta z$, is easily rewritten as

$$g_n(r) = \lim_{Z \rightarrow \infty} \int_{-Z}^{Z} d\zeta \frac{2}{\sqrt{r^2 + \zeta^2}} \cos(n\omega\zeta) \qquad (A6)$$

This integral is the real part of a complex integral $g_n^*(r)$:

$$g_n^*(r) = \lim_{Z \to \infty} \int_{-Z}^{Z} d\zeta \frac{2}{\sqrt{r^2 + \zeta^2}} \exp(in\omega\zeta) \qquad (A7)$$

(where $i = \sqrt{-1}$) which is part of a contour integral in the complex plane, CI_1, of which the other terms are (see figure A1)

$$
\begin{array}{llll}
CI_2: & \zeta = Ze^{i\gamma} & \gamma: & 0 \to 1/2\pi - \varepsilon \\
CI_3: & \zeta = \delta + iru & u: & (Z/r)\cos(\varepsilon) \to 1 \\
CI_4: & \zeta = ir + \delta e^{-i\gamma} & \gamma: & 0 \to \pi \qquad\qquad (A8) \\
CI_5: & \zeta = -\delta + iru & u: & 1 \to (Z/r)\cos(\varepsilon) \\
CI_6: & \zeta = Ze^{i\gamma} & \gamma: & 1/2\pi + \varepsilon \to \pi
\end{array}
$$

where $\delta = Z\sin(\varepsilon)$ and ε is defined such that δ approaches zero when Z goes to infinity (e.g., $\varepsilon = r^2/Z^2$). It is easily verified that the second, fourth, and sixth contours yield zero in the limit for $Z \to \infty$. For the second and sixth contour integrals the value close to the real axis is of order Z^{-1}, and it decreases exponentially for increasing imaginary values in the complex plane. The fourth contour integral is an integra-
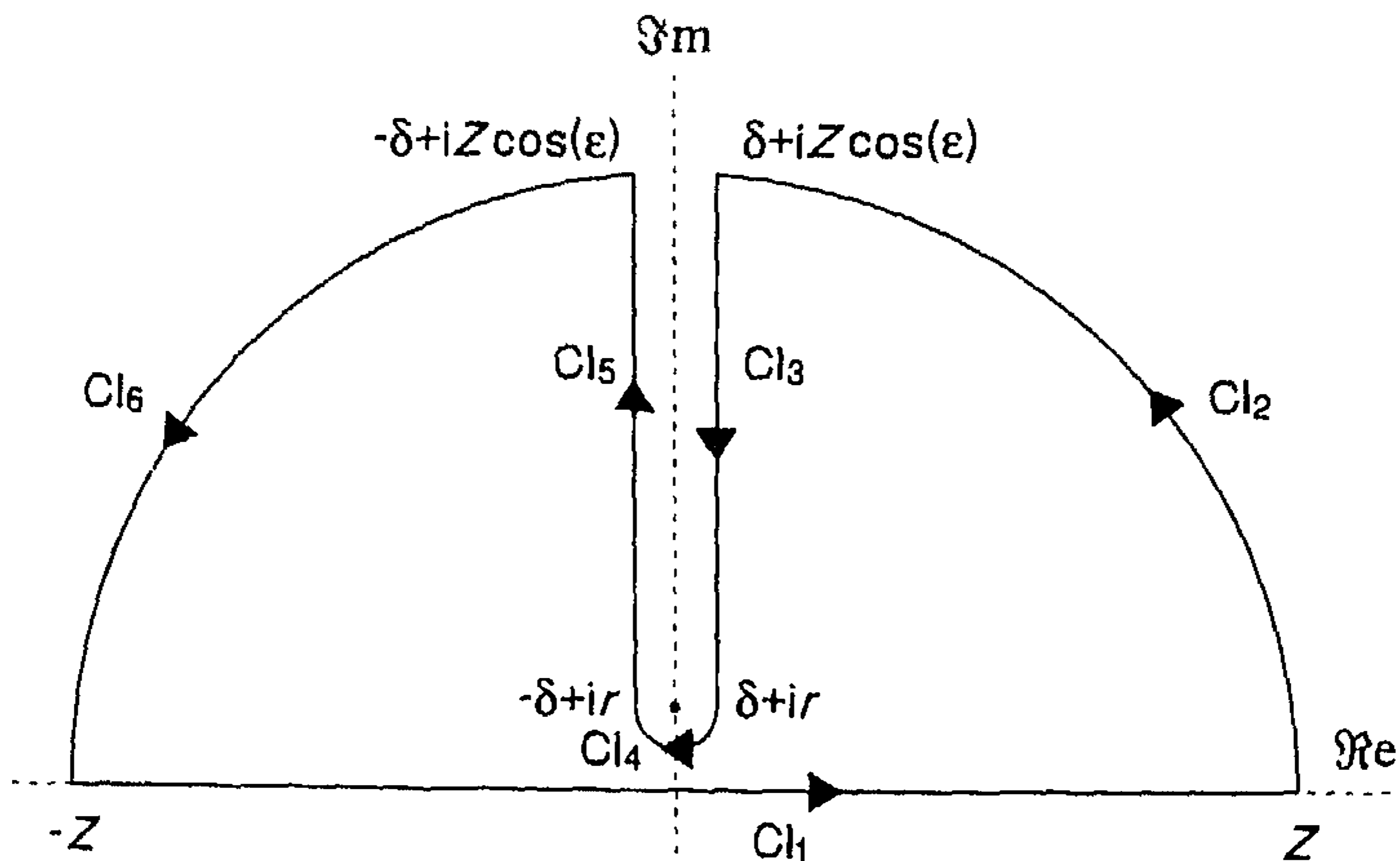

FIG. A1. Contour of integration $(CI_1 - CI_6)$ used for calculating $g_n^*(r)$ in the complex plane; real and imaginary axes denotes by $\Re$e and $\Im$m, respectively. Other symbols are defined in the text.

tion over path length δ of a function of order $\delta^{-1/2}$. For the third contour,

$$CI_3 = \lim_{\substack{\delta \to 0 \\ Z \to \infty}} \int_{(Z/r)\cos(\varepsilon)}^{1} ir\,du \frac{2\exp(in\omega[\delta + iru])}{\sqrt{r^2 + \delta^2 + 2i\delta ru - r^2 u^2}} \qquad (A9)$$

In the limits:

$$CI_3 = -2\int_{1}^{\infty} du \frac{\exp(-n\omega ru)}{\sqrt{u^2 - 1}} \qquad (A10)$$

which is equal to $-2K_0(n\omega r)$ according to the integral representation definition of this modified Bessel function [12]. The same procedure can be followed for the fifth contour, yielding the same result, so that for the sum of contours,

$$\lim_{N \to \infty} (CI_1 + CI_2 + CI_3 + CI_4 + CI_5 + CI_6) = g_n^*(r) + 4K_0(n\omega r) \qquad (A11)$$

Now $K_0(n\omega r)$ is a real function, with imaginary part zero, and realizing that the full contour integral must be zero, it immediately follows that

$$g_n(r) = g_n^*(r) = 4K_0(n\omega r) \qquad (A12)$$

For calculation of the zero order function term $g_0(r)$ we have

$$g_0(r) = \frac{1}{\Delta z} \int_{-(1/2)\Delta z}^{(1/2)\Delta z} dz'' F_{S,\infty}(r, z'') \qquad (A13)$$

where again z'' is the integration variable. Following the same procedure as for (A2) we derive

$$g_0(r) = \lim_{N \to \infty} \left[\sum_{i=-N}^{N} \int_{-(1/2)\Delta z}^{(1/2)\Delta z} dz'' \frac{1}{\sqrt{r^2 + (z'' - i\Delta z)^2}} \right.$$

$$\left. - \sum_{i=-N}^{N} \int_{-(1/2)\Delta z}^{(1/2)\Delta z} dz'' \frac{1}{\sqrt{r_c^2 + (i\Delta z)^2}} \right] \qquad (A14)$$

The lefthand terms can be treated as above, substituting $\zeta = z'' - i\Delta z$ and $Z = (N + 1/2)\Delta z$, transforming into a limit for $Z \to \infty$. The righthand terms are not worked out here, but each individual term is a

constant, so the summation can be expressed as a constant G_Z and we derive

$$g_0(r) = \lim_{Z \to \infty} \left[\int_{-Z}^{Z} d\zeta \frac{1}{\sqrt{r^2 + \zeta^2}} - G_Z \right] \tag{A15}$$

The integral term is symmetric, so it is equal to twice the integral over $0 \to Z$, which is easily solved:

$$g_0(r) = \lim_{Z \to \infty} \left[2\left[\ln\left(\zeta + \sqrt{r^2 + \zeta^2} \right) \right]_0^Z - G_Z \right] \tag{A16}$$

yielding

$$g_0(r) = \lim_{Z \to \infty} \left[2\ln\left(Z + \sqrt{r^2 + Z^2} \right) - 2\ln(r) - G_Z \right] \tag{A17}$$

Since the limit value must be finite, this can be expressed as

$$g_0(r) = g_{01} - \ln(r^2) \tag{A18}$$

where g_{01} is the limit constant yet to be found. Substituting these $g_n( )$ into equation (A1), $F_{S,\infty}(r, z)$ can be written as

$$F_{S,\infty}(r, z) = g_{01} - \ln(r^2) + \sum_{n=1}^{\infty} 4K_0(n\omega r)\cos(n\omega z) \tag{A19}$$

and finally the constant g_{01} can be found from the boundary condition $F_{S,\infty}(r_c, 0) = 0$, which leads to (8).

APPENDIX B: SOLUTION FOR THE CORRECTION FUNCTION TERM

The differential equation (13) is for any value of z', so the individual terms in this series can be isolated:

$$\left(\nabla_r^2 - n^2\omega^2 \right)f_{cn}(r) + \frac{n\omega v}{D}f_{sn}(r) = 0 \qquad n \geqslant 0 \tag{A20}$$

$$-\frac{4n\omega v}{D}K_0(n\omega r) + \left(\nabla_r^2 - n^2\omega^2 \right)f_{sn}(r) - \frac{n\omega v}{D}f_{cn}(r) = 0 \qquad n \geqslant 0 \tag{A21}$$

for $n = 0$, the $f_{s0}(\ )$ is redundant, and the $f_{c0}(\ )$ can easily be solved as

$$f_{c0}(r) = a_0 + a_1 \ln\left(\frac{r^2}{r_c^2}\right) \tag{A22}$$

with integration constants a_0 and a_1. For $n \geqslant 1$, the solutions for $f_{cn}(\ )$ and $f_{sn}(\ )$ can be straightforwardly obtained as combinations of the modified Bessel functions $I_0(\ )$ and $K_0(\ )$:

$$f_{cn}(r) = b_{0n}I_0(\lambda_n r) + b_{1n}I_0(\overline{\lambda}_n r) + c_{0n}K_0(\lambda_n r)$$

$$+ c_{1n}K_0(\overline{\lambda}_n r) - 4K_0(n\omega r) \tag{A23}$$

$$f_{sn}(r) = -ib_{0n}I_0(\lambda_n r) + ib_{1n}I_0(\overline{\lambda}_n r)$$

$$- ic_{0n}K_0(\lambda_n r) + ic_{1n}K_0(\overline{\lambda}_n r) \tag{A24}$$

where the coefficients are complex values (including $i = \sqrt{-1}$) and $\overline{\lambda}_n$ is the complex conjugate of λ_n, which follows from

$$\left(\lambda_n^2 - n^2\omega^2\right) - \frac{in\omega v}{D} = 0 \tag{A25}$$

The solution for λ_n is presented in (17).

Concerning the boundary conditions, for (11) it can be stated that the solution $F_\varepsilon(r,z,t)$ has to remain finite for both small and large r. For large r (i.e., "from far away"), the individual sources no longer can be discerned. Consequently, neither can their movement, and the resulting local O_2 flux field is independent of the particular model used, $F_{S,\infty}(\ )$ or $F_T(\ )$. This is mathematically expressed as

$$\lim_{r \to \infty} \vec{\nabla}F_\varepsilon(r,z,t) = \vec{0} \tag{A26}$$

Applied to (A22)–(A24), this implies that $a_1 = b_{0n} = b_{1n} = 0$.

For $r \to 0$, $F_\varepsilon(r,z,t)$ must remain finite at least in between the sources. Since all $K_0(..r)$ approach $-\ln(r) + Constant$ [12], the sum of the respective coefficients in (A23) and (A24) has to be zero:

$$c_{0n} + c_{1n} - 4 = 0; \quad -ic_{0n} + ic_{1n} = 0 \tag{A27}$$

yielding

$$c_{0n} = c_{1n} = 2 \qquad (A28)$$

Inserting these values for the coefficients in (A22)–(A24) leads to (14)–(16).

APPENDIX C: EQUIVALENT ERYTHROCYTE DIMENSIONS

The point sources are to represent erythrocytes, but these have finite dimensions, whereas a point source does not. Oxygen is assumed to be released from the erythrocyte at a certain pressure p_E, and the equivalent boundary condition for the point source is that it represents this pressure value at a certain location $(r, z') = (r_E, z_E)$ yet to be determined. With the stroboscope method [1], a single point source at $\vec{r}_i = 0$ adds a term $V / |\vec{r}|$ to the expression for p that is spherically symmetric. Exactly the same term arises for a spherical source, that is, a homogeneous distribution of sources over a sphere. Thus, the equivalent location for the respective boundary condition was taken to be the radius of a sphere with the same volume as the erythrocyte:

$$r_{sE} = \left(\frac{3V_E}{4\pi} \right)^{-1/3} \qquad (A29)$$

where V_E is the erythrocyte volume and r_{sE} is the radius of the sphere. Notably, the boundary condition was taken at $(r_{sE}, 0)$, which was close to the capillary border.

A single moving source has to obey (1) and (2), where the directions z and r are not equivalent, and consequently its contribution to the solution for p is no longer spherically symmetric. A possible solution to the describing equations for a moving source is

$$F_1(r, z') = F_{00} + \frac{F_{10}}{\sqrt{r^2 + z'^2}} \exp\left\{ -\frac{v}{2D} \left(z' + \sqrt{r^2 + z'^2} \right) \right\} \qquad (A30)$$

as can be verified by substitution in the equations using $p = Q/(4\mathcal{P})\{\Psi_\infty + R^2 F_1\}$ similar to (9) and following; F_{00} and F_{10} are arbitrary constants. This solution is pointlike (infinite value when approaching the source location $r \to 0$, $z' \to 0$) and in the limit for $v/D \to 0$ changes into the nonmoving point-source equation. More importantly, in the cases covered here it seems to resemble $F_T(\ )$ quite well for small values of r and z' around a single source. Therefore, we assume that the moving-source boundary conditions can be found from this function, in the same way as for the nonmoving sources [1]. This

means that we try to find a volume measuring V_E with a shape, not be confused with the erythrocyte shape, that is defined such that over its whole boundary the function has a fixed value F_{11}, that is,

$$F_{11} = F_{00} + \frac{F_{10}}{\sqrt{\rho^2 + z'^2}} \exp\left\{ -\frac{v}{2D}\left(z' + \sqrt{\rho^2 + z'^2}\right)\right\} \quad (A31)$$

where (ρ, z') is a point on the surface and ρ depends on z' as stated in the above equation. The latter can be rewritten as

$$\ln\left(\frac{F_{10}}{F_{11} - F_{00}}\right) = 1/2\ln(\rho^2 + z'^2) + \frac{v}{2D}\left(z' + \sqrt{\rho^2 + z'^2}\right) \quad (A32)$$

Figure A2 shows the functional dependence of ρ and z' for the situations covered here, a contour that is a cross-section to the surface of the shape. For $\rho = 0$, there are two values of z', a minimum $(z_0 < 0)$
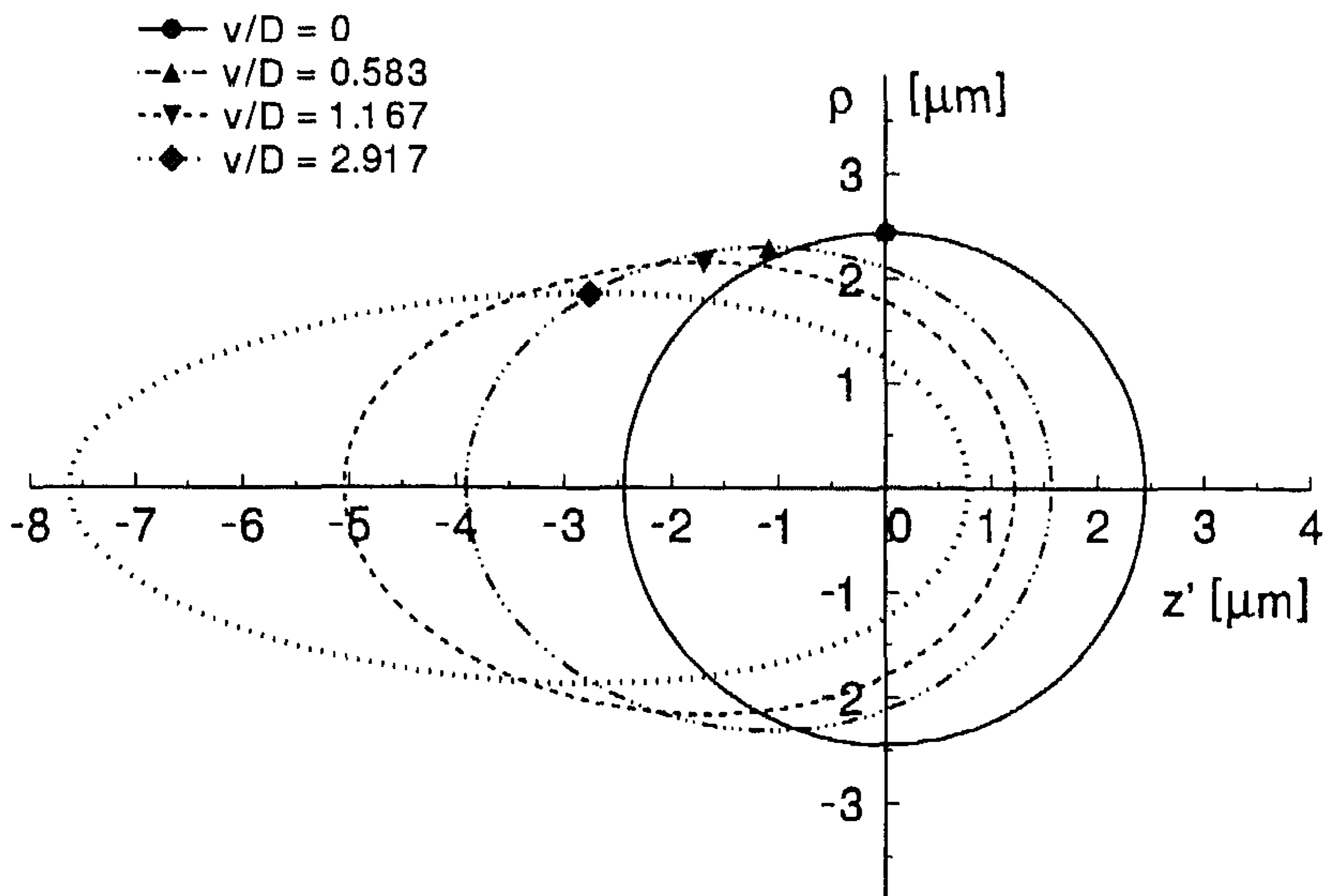

FIG. A2. Outlines of the equivalent source shapes calculated from (A32) for the values of v/D as indicated; the shape is circularly symmetric around the z'-axis, and the figure shows the cross-section along this axis. The symbols indicate the locations (r_E, z_E).

and a maximum $(z_1 > 0)$ distance on the z'-axis ('tail' and 'head' of the contour):

$$\ln\left(\frac{F_{10}}{F_{11} - F_{00}}\right) = \ln(-z_0) = \ln(z_1) + (v/D)z_1 \qquad \text{(A33)}$$

and consequently the volume of the shape can be calculated as

$$V_E = \int_{z_0}^{z_1} dz'\pi\rho^2 \qquad \text{(A34)}$$

To solve this equation, we use an integration variable $s = \sqrt{(\rho^2 + z'^2)}$, which ranges from $s = -z_0$ (for $z' = z_0$) to $s = z_1$ (for $z' = z_1$). According to (A32),

$$0 = \frac{ds}{s} + \frac{v}{2D}(dz' + ds) \qquad \text{(A35)}$$

Now in (A34) we substitute $s^2 - z'^2$ for ρ^2, accordingly split the integration in two parts, and in the left part replace the integration over dz' by ds as solved from (A35):

$$V_E = -\int_{-z_0}^{z_1}\left(1 + \frac{2D}{vs}\right)ds\pi s^2 - \int_{z_0}^{z_1}dz'\pi z'^2 \qquad \text{(A36)}$$

This can be solved straightforwardly:

$$V_E = \pi\left(\frac{D}{v}\left(z_0^2 - z_1^2\right) - \frac{2}{3}z_1^3\right) \qquad \text{(A37)}$$

Also using (A29) and (A33), this yields (25).

With the stroboscope model, the boundary condition used was for the location that extended most towards the tissue $-(r_{sE}, 0)$. Here, the maximum extension from the z' axis is found for $d\rho/dz' = 0$, and denoting this location by $(\rho, z') = (r_E, z_E)$, we derive from (A32)

$$0 = \frac{z_E}{r_E^2 + z_E^2} + \frac{v}{2D}\left(1 + \frac{z_E}{\sqrt{r_E^2 + z_E^2}}\right) \qquad \text{(A38)}$$

Note that (r_E, z_E) also has to obey (A32) itself. This set of equations is more easily solved for $s_E = \sqrt{(r_E^2 + z_E^2)}$, leading to

$$\ln\left(\frac{F_{10}}{F_{11} - F_{00}}\right) = \ln(s_E) + \frac{(v/D)s_E}{2 + (v/D)s_E} \qquad \text{(A39)}$$

This equation, combined with (A33), leads to (26). Equation (27) is easily verified for z_E from (A38) and for r_E from $r_E = \sqrt{(s_E^2 - z_E^2)}$. In Figure A2, also, the locations (r_E, z_E) are indicated; s_E is the distance of this location from the origin.

REFERENCES

1 C. Bos, L. Hoofd, and T. Oostendorp, Mathematical model of erythrocytes as point-like sources, *Math. Biosci.* 125:165–189 (1995).

2 A. Krogh, The number and distribution of capillaries in muscles with calculations of the oxygen pressure head necessary for supplying the tissue, *J. Physiol.* 52:409–415 (1919).

3 L. Hoofd, Updating the Krogh model: Assumptions and extensions, in *Oxygen Transport in Biological Systems*, S. Egginton and H. F. Ross, eds., Cambridge University Press, Cambridge, UK, 1992, pp. 197–229.

4 Z. Turek, L. Hoofd, and K. Rakušan, Myocardial capillaries and tissue oxygenation, *Can. J. Cardiol.* 2:98–103 (1986).

5 L. Hoofd, J. Olders, and Z. Turek, Oxygen pressures calculated in a tissue volume with parallel capillaries, in *Oxygen Transport to Tissue XII*, J. Piiper, T. K. Goldstick, and M. Meyer, eds., Plenum Press, New York, 1990, pp. 21–29.

6 P. L. Altman, J. F. Gibson, and C. C. Wang, in *Handbook of Respiration*, D. S. Dittmer and R. M. Grebe, eds., W. B. Saunders Co., Philadelphia, 1958, p. 102.

7 K. Akmal, D. F. Bruley, N. Banchero, R. Artigue, and W. Maloney, Multicapillary model for oxygen transport to skeletal muscle, in *Oxygen Transport to Tissue III*, A. Silver, M. Erecińska, and H. I. Bicher, eds., Plenum Press, New York, 1978, pp. 139–147.

8 K. Groebe and G. Thews, Effects of red cell spacing and red cell movement upon oxygen release under conditions of maximally working skeletal muscle, in *Oxygen Transport to Tissue XI*, K. Rakusan, G. P. Biro, T. K. Goldstick, and Z. Turek, eds., Plenum Press, New York, 1989, pp. 175–185.

9 K. Rakušan and J. Rajhathy, Distribution of cardiac output and organ blood content in anemic and polycythemic rats, *Can. J. Physiol. Pharmacol.* 50:703–710 (1972).

10 A. G. Tsai and M. Intaglietta, Local tissue oxygenation during constant red blood cell flux: A discrete source analysis of velocity and hematocrit changes, *Microvas. Res.* 37:308–322 (1989).

11 A. G. Tsai and M. Intaglietta, Evidence of flowmotion induced changes in local tissue oxygenation, *Int. J. Microcirc: Clin. Exp.* 12:75–88 (1993).

12 M. Abramowitz and I. A. Stegun, *Handbook of Mathematical Functions*, Dover, New York, 1965.